Electronic Supplementary Material (ESI) for Physical Chemistry Chemical Physics.
This journal is © the Owner Societies 2021

Supporting Information For "The Redox Potential of a Heme Cofactor in Nitrosomonas europaea Cytochrome c Peroxidase: A Polarizable QM/MM Study"

Elizabeth A. Karnaukh,[a] and Ksenia B. Bravaya*[a]

[a]Department of Chemistry, Boston University, Boston, Massachusetts 02215, USA

Contents

S1. COMPUTATIONAL DETAILS

A. CHARMM Force Field Parameters

While the parameters describing Fe-Porphyrin and Fe-His interactions are available in the standard CHARMM27 forcefield, [1, 2] the parameters for the Met-Heme ligation had to be incorporated manually. The equilibrium dihedral angle $\phi_0^{CT3-S-Fe-NPH}$ as well as the force constants K_b^{Fe-S}, $k_\phi^{CT2-S-Fe-NPH}$, and $k_\phi^{CT3-S-Fe-NPH}$ were taken from Ref. [3]. All other equilibrium bond lengths, valence angles, and dihedral angles were adopted from the X-ray crystal structure [4]. Apart from the three force constants taken from Ref. [3] all other force constants associated with Fe-S ligation were considered equal to 0.

TABLE S1: Bond stretch terms in Met-Heme ligation

atom types	b_0 (nm)	K_b (kJ/mol nm^2)
S-Fe	0.233	125520 [3]

TABLE S2: Bond angle and 1,3 Urey-Bradley coupling terms in Met-Heme ligation

atom types	θ_0 (deg)	K_θ (kJ/mol rad^2)	s_0 (nm)	k_{UB} (kJ/mol nm^2)
CT2-S-Fe	117.73	0.0	0.343	0.0
CT3-S-Fe	122.09	0.0	0.442	0.0
NR2-Fe-S	173.89	0.0	0.306	0.0
S-Fe-NPH	88.43	0.0	0.306	0.0

All information about special connectivity between residues, including covalently-bound Cysteines and His-/Met-coordination was incorporated into the specbond.dat file in GROMACS [5].

B. Heme Charge Distributions

The CHARMM27 forcefield includes all parameters for the ferrous heme, [1] including those for Fe-porphyrin and Fe-His interactions,[2] which were employed here; however the parameters

TABLE S3: Proper dihedral terms in Met-Heme ligation

atom names	ϕ_s (deg)	k_ϕ (kJ/mol)	periodicity	atom names	ϕ_s (deg)	k_ϕ (kJ/mol)	periodicity
CPH2-NR2-Fe-S	-161.75	0.0	1	CT2-S-Fe-NR2	75.57	0.0	1
CPH1-NR2-Fe-S	12.1	0.0	1	CT2-S-Fe-NPH	6.225	0.1674 [3]	4
CT3-CT2-S-Fe	-109.32	0.0	1	CT3-S-Fe-NR2	-166.17	0.0	1
HA-CT2-S-Fe	70.56	0.0	1	CT3-S-Fe-NPH	-11 [3]	0.1674 [3]	4
Fe-S-CT3-HA	55.25	0.0	1				

for the ferric heme are not available. The geometric parameters (bond length, valence angles, dihedral angles, etc.) for the ferric heme were considered equal to those of the ferrous heme as each QM/BioEFP vertical energy calculation was preceded by a local QM/MM optimization. The changes in the partial charges from oxidized to reduced state are expected to significantly affect the heme-protein interaction.

In order to obtain the partial charges for the ferric heme, the following procedure has been used. Natural bond orbital (NBO) charges were computed for oxidized and reduced states of the bare FeP molecule in the gas-phase at the ωB97X-D/6-31G(d) level of theory in Q-Chem [6]. The partial charges for all atoms in ferric heme were then computed by adding the difference in NBO charges between ferric and ferrous states to the CHARMM27 ferrous heme partial charges (Eq. S1). Bare FeP and heme *c* differ in their substituents, but they share methine bridge H atoms. The partial charges on heme substituents were considered the same for ferric and ferrous state. The total change in the partial charges between ferric and ferrous FeP for eight H atoms present in the model FeP molecule and absent in the actual heme (due to the substituents) were distributed evenly across the atoms in the porphyrin macrocycle.

$$q_i^{FF,ferric} = q_i^{FF,ferrous} + \left(q_i^{NBO,ferric} - q_i^{NBO,ferrous}\right) \tag{S1}$$

The final partial charges for the atoms along the central FeP moiety in ferrous and ferric states appear below (Fig. S1). Partial charges of the substituents are not included, as they were not altered in either redox state from existing CHARMM parameters for heme *c*.

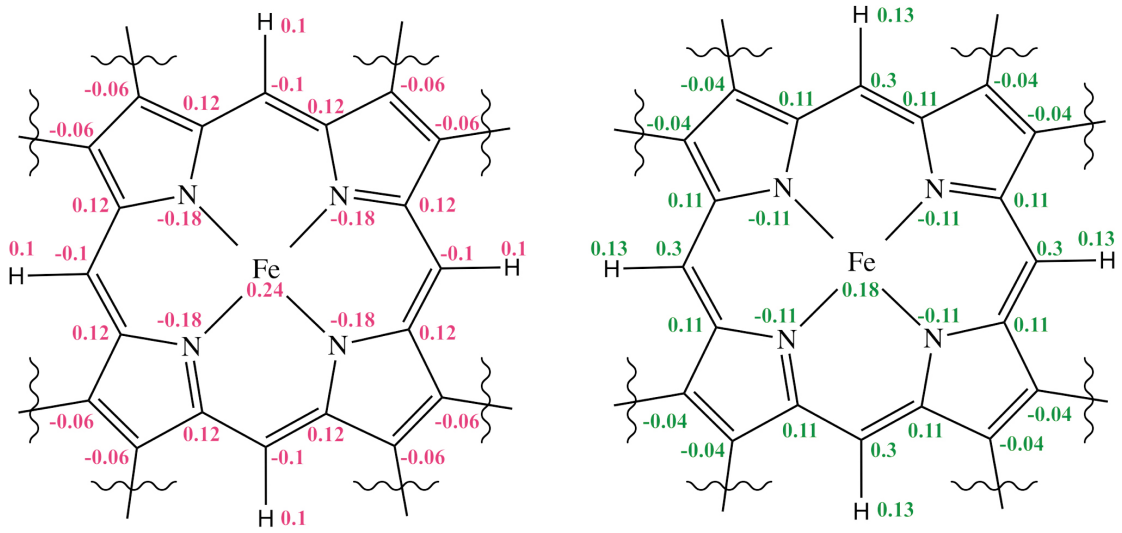

FIG. S1: Distributions of partial charges in ferrous (left, pink) and ferric (right, green) heme in the modified CHARMM27 forcefield.

C. Protonation States Considered

To assign the protonation states of the E146 residue and of the propionic group close to H244, additional MD simulations have been performed. The protonations states that have been considered included deprotonated (E146 DP in Fig. S3) and protonated on either of the oxygen E146 (E146 OE1 and E146 OE2 in Fig. S3). Analysis of the X-ray structure (PDB ID: 1IQC, chain A) shows that there are two H-bonds formed between H244 and COO^- of one of the HP heme's propionic groups (Fig. S2). As follows from the 2.7 Å distance between NH of the H244-backbone and oxygen of the propionic group, there exists a H-bond between the moieties, meaning that the corresponding atom of COO^- group is deprotonated. H244 N_δ atom also forms a H-bond with the other oxygen atom of the COO group as evident from 2.6 Å distance between the corresponding atoms. This points to three possible protonation states for the pair of atoms: (i) COOH and N_ϵ protonated H244 (HISE COOH in Fig. S4), COO^- and N_δ protonated H244 (HISD COO^- in Fig. S4), and finally COO^- and doubly protonated H244 (HISH COO^- in Fig. S4). 10 NPT MD simulations were run to explore each of these cases, and optimal protonation states were chosen based on lowest RMSD values in comparison to the initial, i.e. minimized and equilibrated, structure (Figs. S3 and S4).

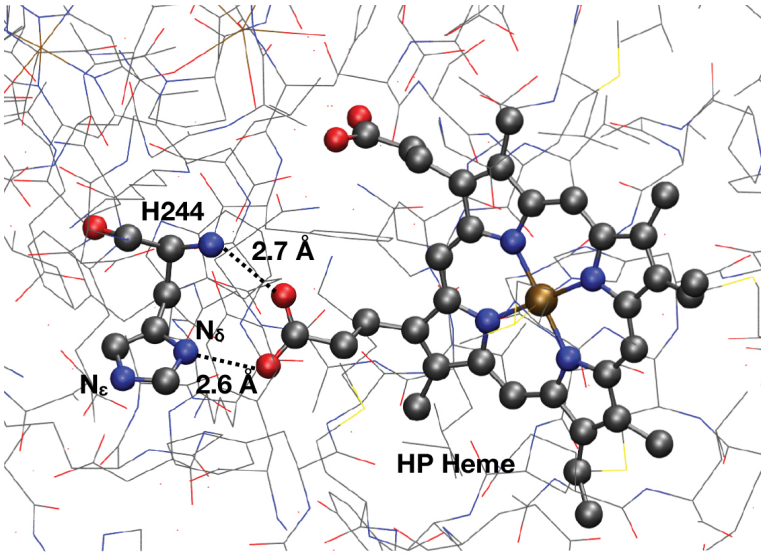

FIG. S2: H-bonds formed between propionic group of HP Heme and H244 (PDB ID: 1IQC, chain A). Only heavy atoms are shown.

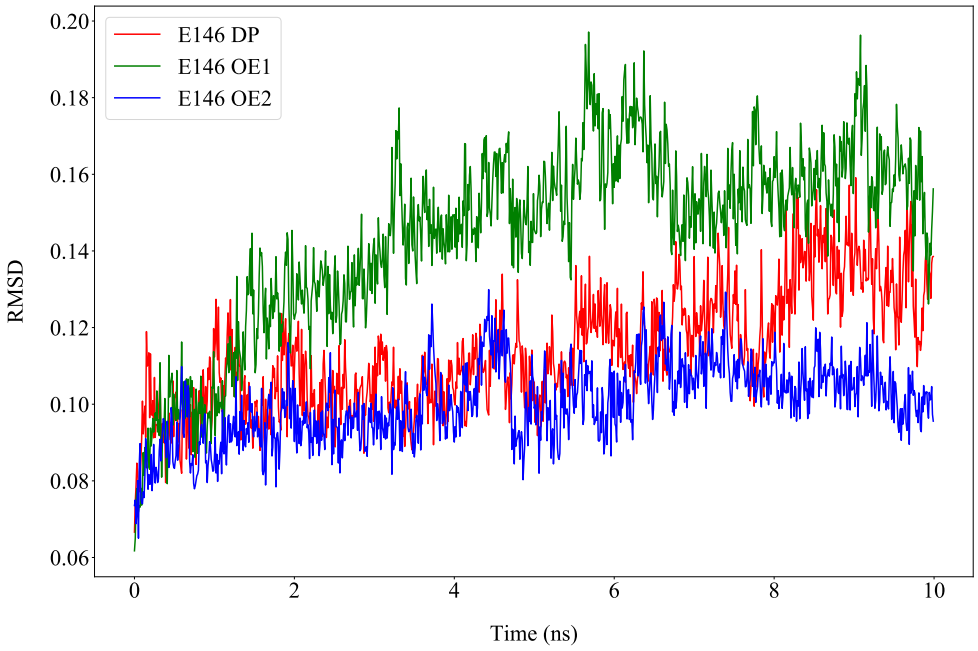

FIG. S3: Root mean squared deviations of MD trajectories where E146 is either left deprotonated, protonated at the first oxygen (OE1), or protonated at the second oxygen (OE2) (computed with GROMACS).

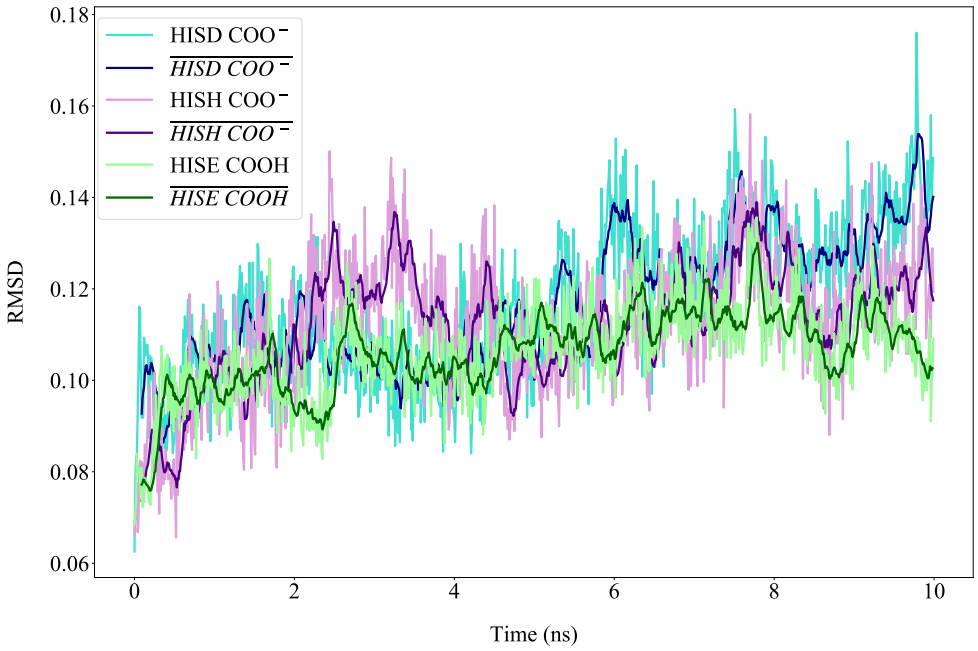

FIG. S4: Root mean squared deviations along the MD trajectories with different protonation states considered for the H244 and one of the heme's propionate groups: COOH and N_ϵ-protonated H244 (HISE COOH), COO^- and N_δ-protonated H244 (HISD COO^-), and finally COO^- and doubly protonated H244 (HISH COO^-). Both bare RMSD and the running average (e.g. $\overline{HISE\ COOH}$) are shown.

S2. CHOICE OF QM/MM BOUNDARY AND LOCAL OPTIMIZATION

A. QM–MM Boundary Used

The final QM subsystem is described below. The QM region consisted of the entire HP heme in addition to Cys 183, Cys 186, His 187, and Met 258 amino acids, all truncated along the C_α–C_β bonds. The link atoms were added in four locations, in between C_α and C_β atoms on each amino acid residue (Figure S5). The propionate closest to H244 was considered protonated due to H-bonding (2.7Å in the X-ray structure, 1IQC) between the propionate oxygen and the N_δ nitrogen of H244 (assuming N_ϵ-protonated H244), as well as the RMSD behaviors explored in Fig. S4). The propionate closest to Y242 was kept deprotonated.

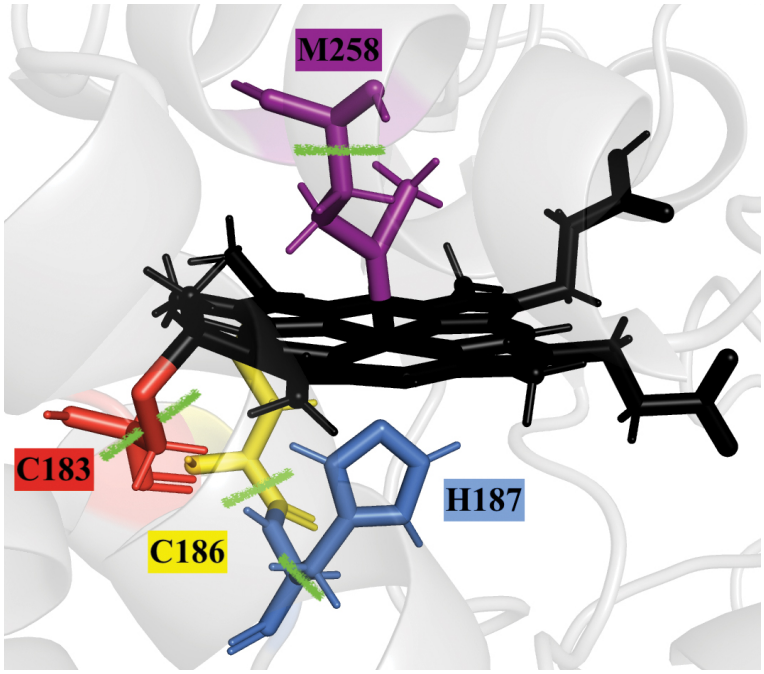

FIG. S5: Final choice of the QM–MM boundary for the HP heme, where link atoms are placed at the bond midpoints indicated in green.

B. QM/MM Local Optimization

The QM/MM local optimization was done in two steps. In the first step, the Fe-S distance was first constrained to 2.3 Å. The resulting coordinates were further used as a starting geometry for the following unconstrained optimization. The $< S^2 >$ value was carefully monitored along

each optimization. 45 out of the 50 snapshots converged to solutions with $< S^2 >$ values $\sim$ 0.75 for the oxidized state. However, for 5 snapshots the $< S^2 >$ values were higher than 1.0.

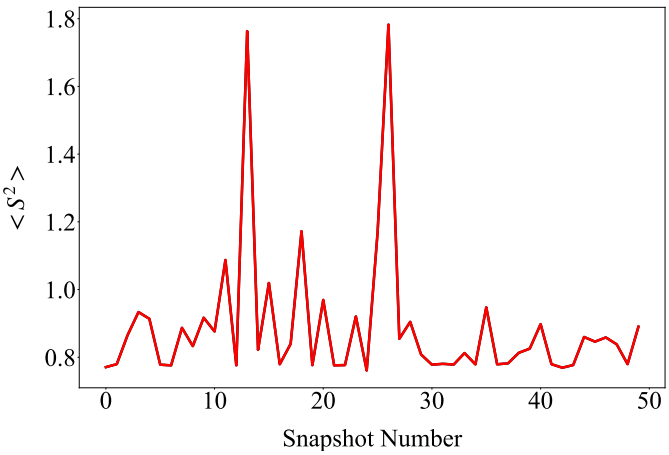

FIG. S6: $< S^2 >$ values for the converged QM/MM locally optimized geometries for the oxidized heme (doublet).

Interestingly, the configurations with the higher values of $< S^2 >$ also exhibited longer Fe-S distances. While the high values $< S^2 >$ obtained in electronic embedding QM/MM used for the geometry optimization were concerning, the $< S^2 >$ expectation values obtained for these geometries in the following QM/BioEFP calculations were all close to 0.75.

S3. QM/BIOEFP PROTOCOL AND RESULTS

A. EFP Parametrization of Non-Standard Fragments

To obtain a reliable representation of the electrostatic environment of the heme, special attention was given to EFP parametrization of the neighboring amino acid moieties. The fragments representing G182, V184, Q185, N188, T257, and G259 were partitioned in a non-standard manner, as indicated below. H capping atoms were added accordingly. While the focus of the current work is on characterizing the redox properties of the HP heme, the LP heme is present in the model and its EFP parameters have to be computed. The fragmentation scheme for the LP is shown in Fig. S7. C39 and C42 were treated as separate fragments from the LP heme; the LP heme was capped in 2 places, while the Cysteines were capped in 3 places. All Ca^{2+} and Mg^{2+} protein ions were treated as separate fragments.

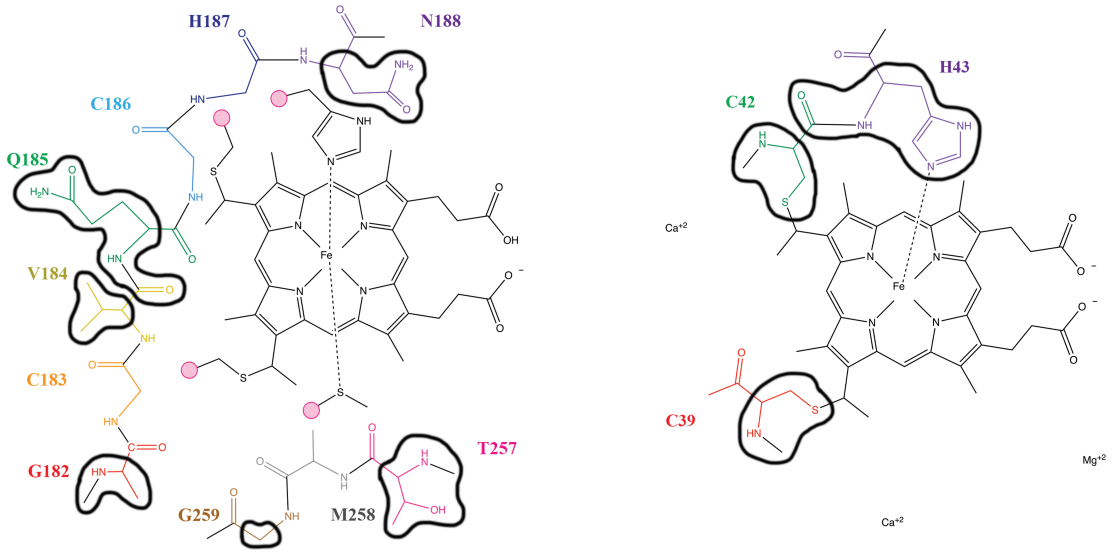

FIG. S7: Scheme defining how the non-standard EFP fragments are cut around the HP heme (left panel) and LP heme (right panel). The left panel represents the QM region and nearby residues; pink atoms represent the link atoms along the QM/MM boundary. All fragments that are not truncated along C_α-C bonds are outlined in black. The right panel represents the LP heme region in addition to protein ions; the LP heme, axial ligand H43, and covalently-bound Cysteines were all treated as separate fragments.

B. QM/BioEFP Densities

While vertical ionization/attachment transitions were observed to occur from charged propionate groups in the gas phase, the differences in ground state densities upon ionization and electron attachment for QM/BioEFP calculations occur on the iron porphyrin moiety. There is no observable difference in the differential ground state densities upon ionization or electron attachment between polarizable and non-polarizable QM/BioEFP methods, indicating that accounting for the environment explicitly through static multipoles is sufficient to recover the correct character of vertical transitions.

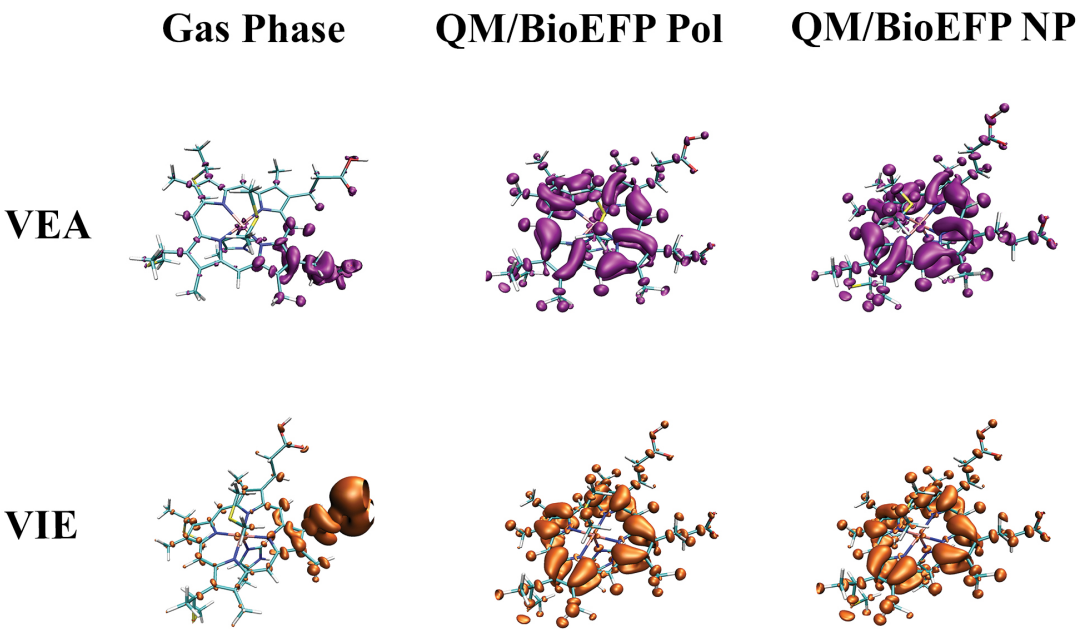

FIG. S8: Ground state differential electron densities upon ionization (top row) or electron attachment (bottom row). Densities were computed as $\rho_{ox}^{VEA} = \rho_{ox}^{red} - \rho_{ox}^{ox}$ and $\rho_{red}^{VIE} = \rho_{red}^{ox} - \rho_{red}^{red}$, where the subscripts represent the redox states corresponding to the optimized geometries, while the superscripts represent the redox states for the evaluated density. Isosurface values are 0.001 for VEA and -0.001 for VIE.

C. Basis Set Correction to Vertical Energy Gaps

The basis set corrections (BSCs) to the VEGs were included by first computing the difference in VEGs upon increasing the basis set to 6-311G(d,p) / LANL2DZ for one snapshot. Assuming this correction is additive, this difference was then added to all VEGs of other snapshots to yield corrected ensemble averaged values (Eq. S2).

$$\begin{aligned} \Delta VEG^{BSC} &= VEG^{6-311G(d,p)/LANL2DZ} - VEG^{6-31G(d)/LANL2DZ} \\ < VEG >^{BSC} &= < VEG >^{6-31G(d)/LANL2DZ} + \Delta VEG^{BSC} \end{aligned} \tag{S2}$$

D. Thermal Correction to Oxidation Free Energy

Provided that the geometries of the HP heme were locally optimized in the presence of a frozen protein environment, the computed vertical energy gaps did not contain contributions from the thermal fluctuations of nuclear degrees of freedom. To estimate this contribution in the gas-phase, a model system of iron porphyrin with truncated Histidine and Methionine ligands (Fig. S9) was used. Vibrational and thermochemical analysis was conducted for oxidized and reduced states of FePHisMet (Eq. S3). Contributions to $\Delta_r G^{thermo}_{gas}$ are included in Tab. S3 D.

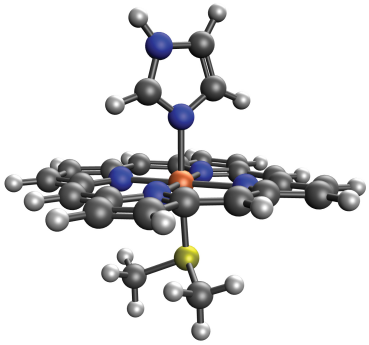

FIG. S9: Model FePMetHis compound.

$$\begin{aligned} \Delta_r G^{LRA} &= \Delta_r G^{LRA,f,BSC} + \Delta\Delta G^{f}_{solv} + \Delta ZPVE + \Delta_r G^{thermo}_{gas} \\ \Delta_r G^{thermo}_{gas} &= \Delta H - T\Delta S \end{aligned} \tag{S3}$$

TABLE S4: ΔH, ΔS, change in the zero-point vibrational energies ($\Delta ZPVE$), and the thermal correction ($\Delta_r G^{thermo}$) to the oxidation free energy of model heme at T=298.15 K.

		Fe(II)HisMet	$\rightleftharpoons$ **Fe(III)HisMet**$^+$
ΔH, eV	ΔS, meV/K	ΔG^{thermo}, eV	$\Delta G^{thermo} + \Delta ZPVE$, eV
-0.041	0.029	-0.050	-0.101

S4. DIFFERENTIAL SOLVATION FREE ENERGY CALCULATIONS

A. General Formalism

To account for bulk solvation effects the differential solvation free energies for the oxidized and reduced states of the system have been computed. The calculations have been performed by numerically solving the nonlinear Poisson Boltzmann equation (PBEQ) using DelPhi software [7]. The electrostatic component to the solvation free energy, $\Delta G_E(solvation)$, can be computed as a difference in electrostatic energies between the solvated protein ($G_E(\varepsilon_s, 80)$) and the protein in vacuum ($G_E(\varepsilon_s, 1)$). The dielectric constant of the solute (ε_s) is set to 4.0 (in the case of the protein solvation free energy) [7].

$$\begin{aligned} -\nabla \cdot \varepsilon(x)\nabla\Phi(x) + \bar{\kappa}^2(x) sinh\Phi(x) &= f(x) \\ G_E &= \frac{1}{2}\sum_i q_i \Phi_i \\ \Delta G_E(solvation) &= G_E(\varepsilon_s, 80) - G_E(\varepsilon_s, 4) \end{aligned} \tag{S4}$$

B. Phenolate Anion

The efficacy of DelPhi was tested by exploring differential solvation energies for a single phenolate molecule embedded in spherical water droplet of 30 Å. Differential solvation free energy between reduced and oxidized states ($\Delta\Delta G_{solv}$) of the phenolate molecule in its reduced geometry was computed with DelPhi and compared to the Born solvation free energy $\Delta G_{solv}^{Born} = \frac{Q^2}{2R}(1 - \frac{1}{\epsilon})$, which yields the value of 0.237 eV for the 30 Å ion in water. The DelPhi value of 0.258 eV is in good agreement with the value obtained from the Born solvation model. Partial charges on water molecules were zeroed out for these calculations.

C. NeC*c*P model

The ensemble-averaged differential solvation free energies were computed for 50 snapshots for both oxidized and semi-reduced state geometries of the protein in the 10 Å water shell using DelPhi software [7]. Atomic charges and scaled van der Waals radii were read from assembled PQR files for each snapshot. The resulting value of $\Delta\Delta G_{solv}^{f}$ ($\Delta\Delta G_{solv}^{f} \approx 0.5 \times \left(< \Delta\Delta G_{solv}^{f} >_{Ox} + < \Delta\Delta G_{solv}^{f} >_{Red} \right)$ was 0.236 eV. All partial charges including those for

the QM subsystem, protein, solvent molecules and counterions have been included into the calculation.

D. Heme differential solvation free energy

To explain the minimal role of the environment polarization on the computed values of the Gibbs free energies and of the redox potentials, we have calculated differential solvation free energies of the quantum subsystem only in the dielectric medium representing the protein environment. Indeed, despite the change of the total charge by one upon ionization, the difference in solvation free energy was found to be negligible (see below).

TABLE S5: Differential solvation free energies for the heme model in a dielectric medium representing a protein environment (ε=4). The coordinates are taken from snapshot 3 QM/MM optimized geometries in each trajectory, and the modified force field charges have been used for the solute. DelPhi software [7] has been used.

Heme	ΔG_{solv} (eV)
HP, Ox	0.268
HP, Red	0.249
$\Delta\Delta G_{solv}$ (eV)	
0.019 eV	

S5. ENSEMBLE-AVERAGED VERTICAL ENERGY GAPS

A. Error Analysis

The data used to computed oxidation free energies, solvation energy corrections, and standard reduction potentials are summarized below with standard errors.

TABLE S6:

	QM/BioEFP NP	**QM/BioEFP**
$< \mathbf{VEA} >_{\mathbf{50}}$ **(eV)**	4.46 ± 0.10	4.46 ± 0.13
$< \mathbf{VIE} >_{\mathbf{50}}$ **(eV)**	5.76 ± 0.09	5.81 ± 0.09
$\mathbf{G_{ox}^{LRA,f}(eV)}$	5.11 ± 0.07	5.14 ± 0.08
$\mathbf{\Delta\Delta G_{solv}^{f}(eV)}$	0.24 ± 0.04	0.24 ± 0.04
$\mathbf{\Delta G_{ox}^{LRA}(eV)}$	5.46 ± 0.04	5.49 ± 0.05
$\mathbf{E^{o}}$ **(V)**	1.15 ± 0.04	1.17 ± 0.05

Standard errors were computed as $\Delta = \frac{t(95\%,n-1)\sigma}{\sqrt{n}}$ where t is the Student's t test at a 95% confidence interval, σ is the standard deviation, n is the sample size, and $n = 50$ was used. Probability distributions of $< VIE >$ and $< VEA >$ were fitted with normal distributions. All relevant statistical information is included below.

TABLE S7: Percent errors in means, standard deviations, and variances.

	$< \mathbf{VEA} >_{\mathbf{50}}$ **(eV)**	$< \mathbf{VIE} >_{\mathbf{50}}$ **(eV)**
μ_{exp}	4.462	5.761
μ_{theo}	4.456	5.756
% Error in μ	0.126	0.103
σ_{exp}	0.378	0.331
σ_{theo}	0.378	0.329
σ^2_{exp}	0.143	0.110
σ^2_{theo}	0.143	0.109

B. Histogram Analysis

The bin width (h) and number of bins (k) for VEG histograms were computed according to Scott's Normal Reference Rule[8–10]:

$$h = 3.5\frac{\sigma}{\sqrt[3]{n}}$$
$$k = \frac{max - min}{3.5\frac{\sigma}{\sqrt[3]{n}}} \tag{S5}$$

Other bin parameters were explored according to Sturges' Rule[10, 11], Silverman's Rule[12], and Average Shifted Histograms[13, 14]; resulting histograms are shown below. Choosing more bins according to $k = 1+3.322log(n)$ (Sturges') or a smaller bin width according to $h = 1.06\frac{\sigma}{\sqrt[5]{n}}$ (Silverman's) resulted in less normal distributions.

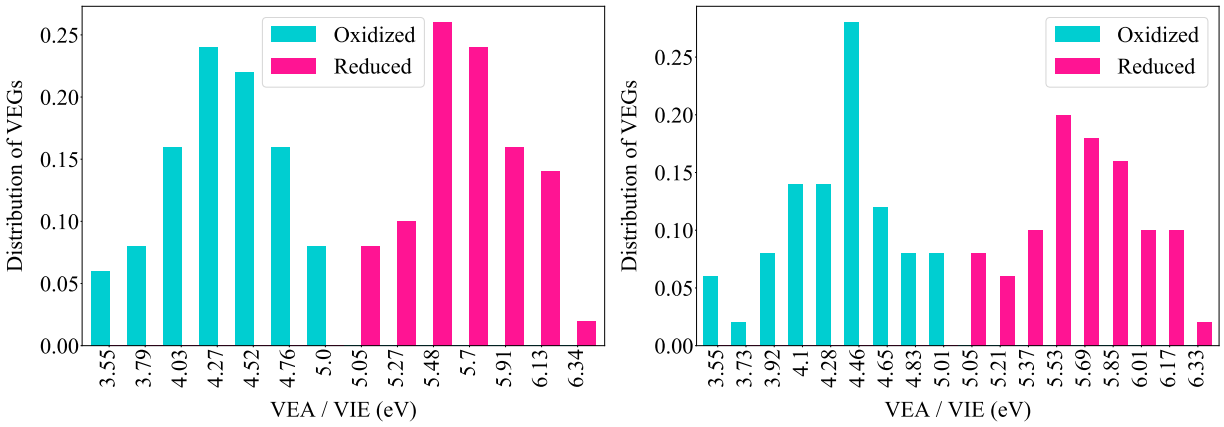

FIG. S10: Histograms generated with bin widths as defined by Sturges' Rule (left) and Silverman's Rule (right); VEAs are in blue, while VIEs are in purple.

Scott's Rule was chosen for final histograms presented in the main text as it is considered to be the optimal choice for distributions that tends towards Gaussian behavior and has been previously used extensively.[15–19]

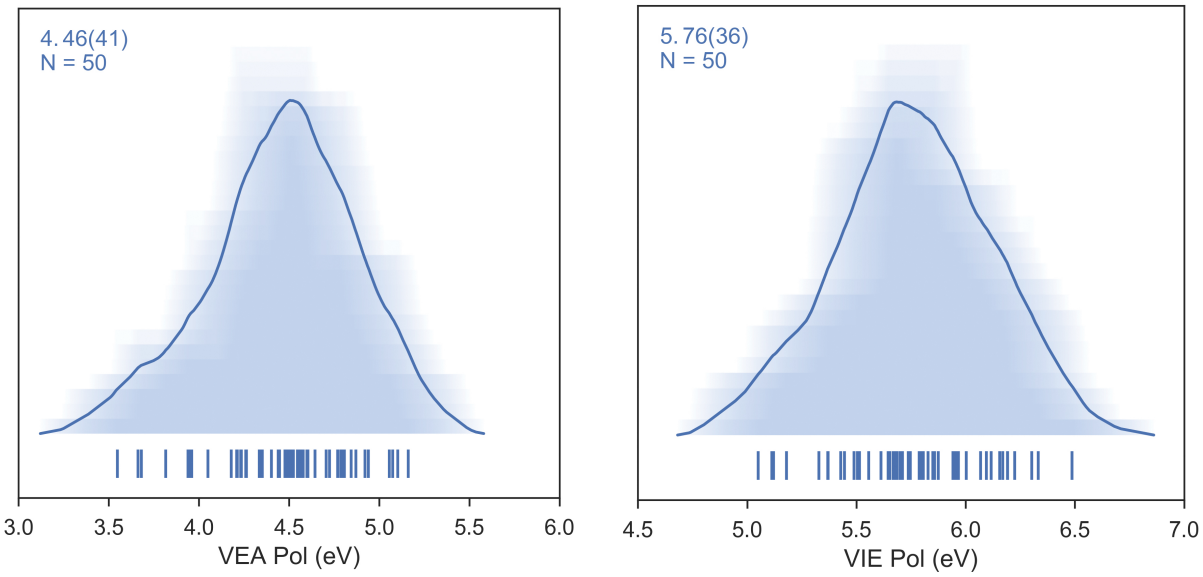

FIG. S11: Average shifted histograms generated with the Buriak Group Data Plotter[14].

S6. HEME PLANARITY ALONG MD TRAJECTORY AND IN QM/MM OPTIMIZED STRUCTURES

To quantify the deviations from the planarity in heme along the MD trajectory and in the QM/MM optimized geometries the four dihedral angles were considered (Fig. S12). The fluctuations of the angles along MD trajectories are shown in Fig. S13. The average values along the trajectory and for 50 QM/MM optimized snapshots are listed in Table S9. One can see that QM/MM optimization does not yield the structures that are substantially more planar.

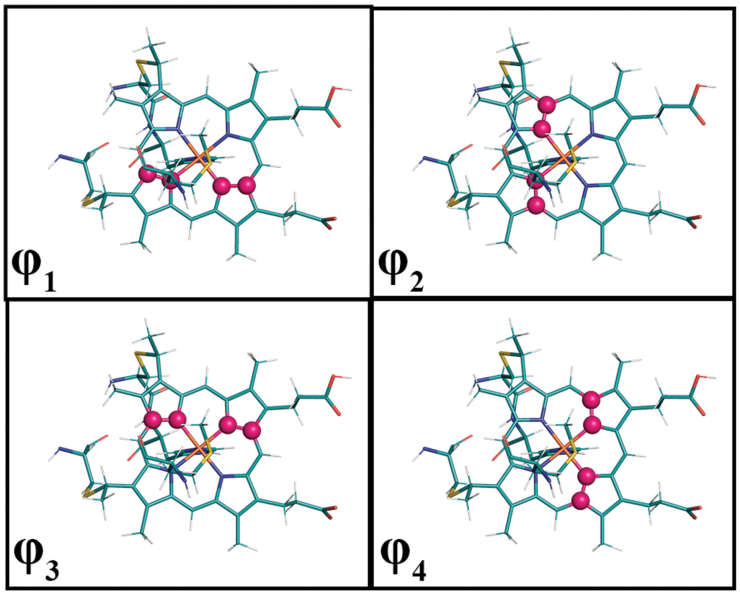

FIG. S12: The four $\phi_{C-N-N-C}$ angles used to quantify the non-planarity of the heme. Carbon and nitrogen atoms are shown in pink.

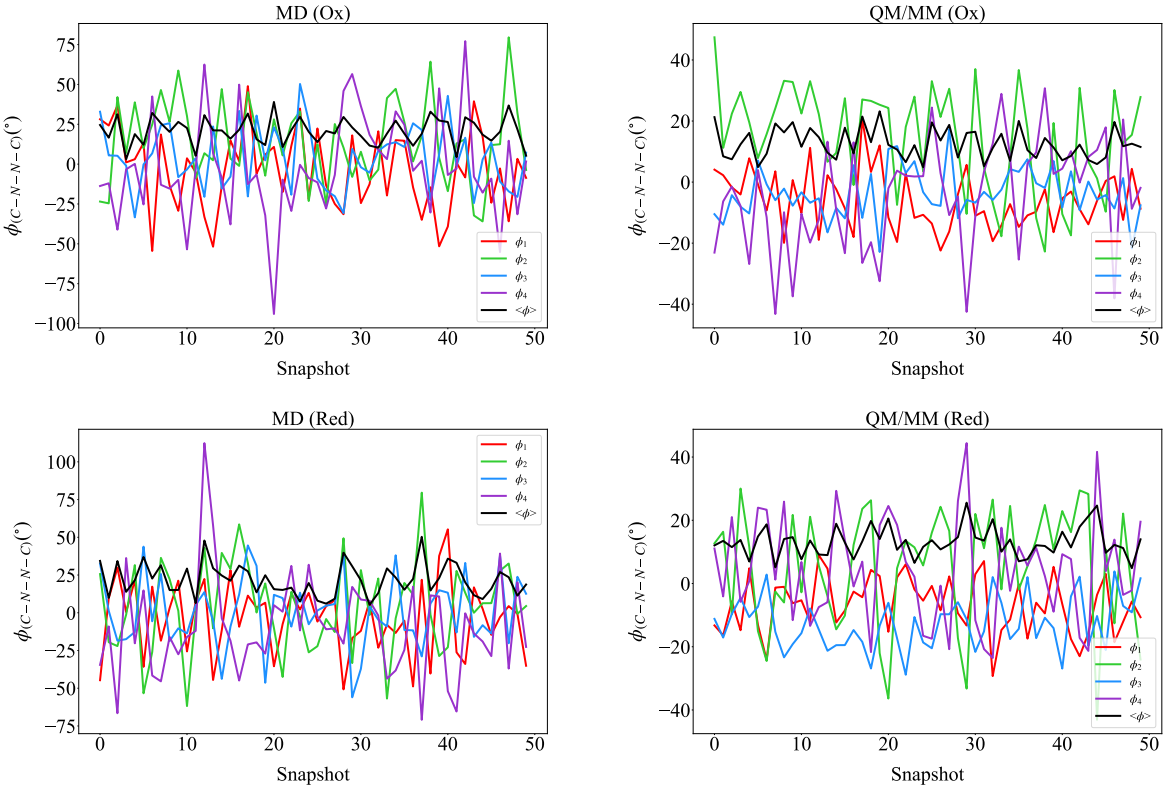

FIG. S13: Fluctuations in individual $\varphi_{C-N-N-C}$ angles over 50 MD and 50 QM/MM optimized geometries.

TABLE S8: Average values of the four dihedral angles defined in Fig. S12 along MD trajectories (oxidized and reduced states), for QM/MM optimized structures, and for the gas phase optimized model.

Angle	Oxidized			Reduced		
	MD	QM/MM	gas phase	MD	QM/MM	gas phase
ϕ_1	-3.96	-5.89	20.52	-4.03	-6.87	18.57
ϕ_2	14.00	14.95	-5.92	4.39	5.18	-11.90
ϕ_3	3.72	-3.61	1.27	0.62	-12.59	-4.70
ϕ_4	-2.20	-4.50	-3.63	-9.50	4.24	4.23

TABLE S9: Average absolute values of the four dihedral angles defined in Fig. S12 along MD trajectories (oxidized and reduced states), for QM/MM optimized structures, and for the gas phase optimized model.

Angle	Oxidized			Reduced		
	MD	QM/MM	gas phase	MD	QM/MM	gas phase
$\|\phi_1\|$	20.33	9.20	20.52	18.80	9.03	18.57
$\|\phi_2\|$	22.98	19.57	5.92	22.97	16.54	11.90
$\|\phi_3\|$	16.11	7.30	1.27	18.57	13.17	4.70
$\|\phi_4\|$	23.47	14.16	3.63	26.41	13.75	4.23

S7. EFFECTS OF HEME GEOMETRIES ON VEG FLUCTUATIONS

Given the well-documented effects of geometric deviations of porphyrin systems on energetic quantities [20–22], several structural parameters were considered to explore correlations between geometrical distortions and computed VEGs. First, the fluctuations of the Fe-S and Fe-N interatomic distances (for Met- and His-coordination, respectively) were investigated. Then, the degree of planarity was measured across snapshots by measuring the average of the absolute values of two θ_{N-Fe-N} angles and four $\phi_{C_\alpha-N-N-C\alpha}$ dihedral angles. Finally, we have looked at the fluctuations of the overall RMSD of the locally-optimized geometries with respect to the crystal structure. We find no correlation between the magnitude of VEGs and the values of these structural parameters (Figs. S14– S17).

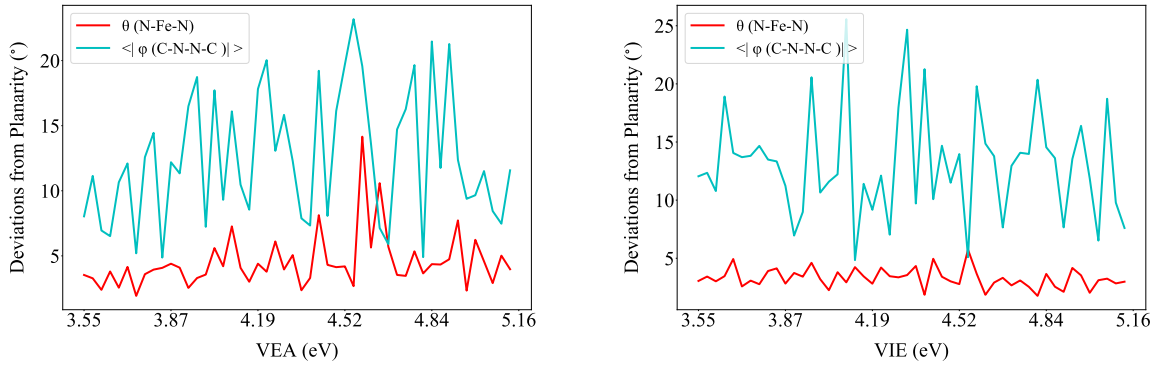

FIG. S14: Deviations of the average of the absolute values of θ angles and ϕ dihedral angles from their values in a planar structure (180° and 0°) plotted with respect to the computed vertical energy gaps.

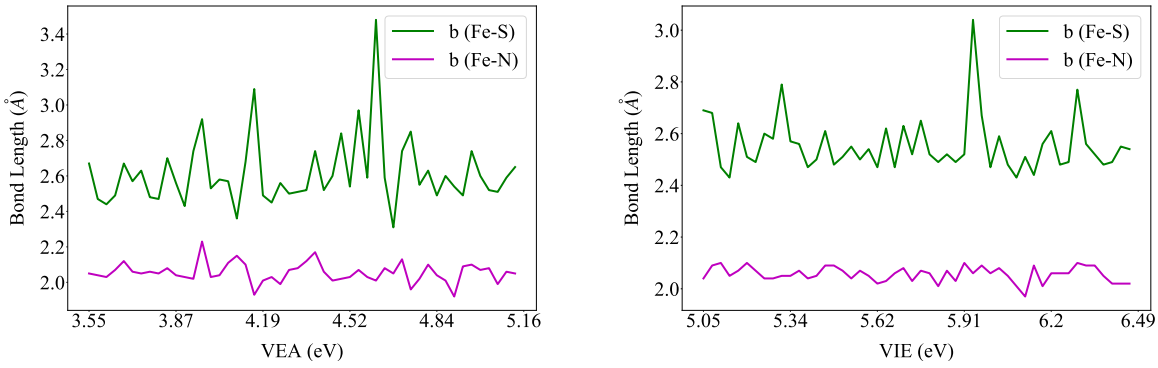

FIG. S15: Deviations of coordination lengths as VEGs increase.

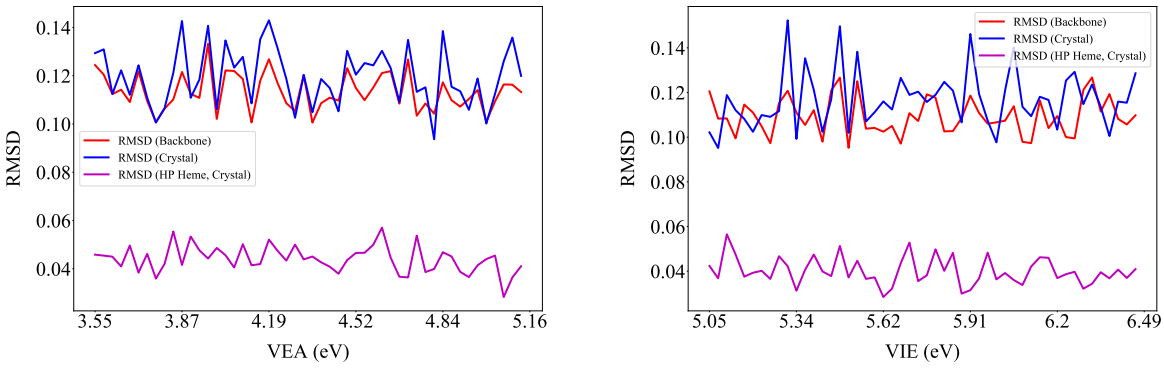

FIG. S16: Root mean square deviations of QM/MM locally optimized geometries with respect to protein backbone, crystal structure, and HP heme as VEGs increase.

In addition, the fluctuations in gas-phase VEGs were compared to those computed with QM/BioEFP. While it was found that VEAs computed in the gas-phase weakly correlated with those obtained with a polarizable environment ($R^2 = 0.22$), the QM/BioEFP VIE fluctuations did not correlate with gas-phase VIE fluctuations.

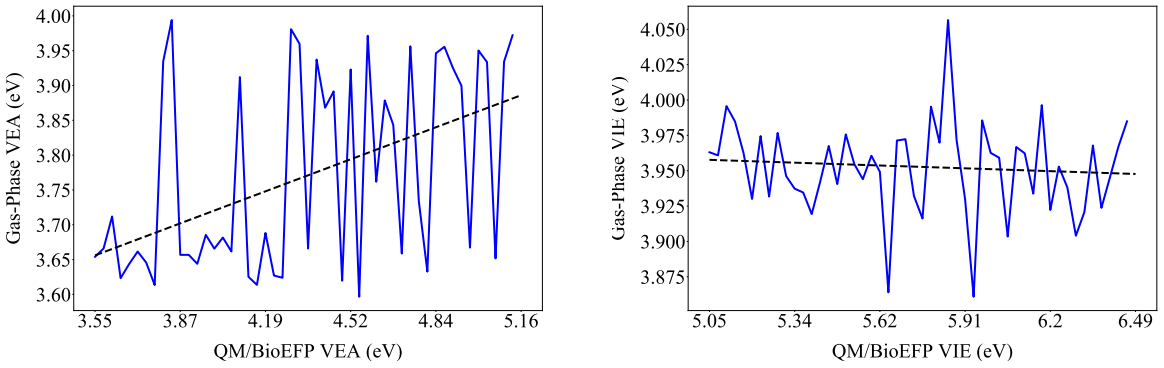

FIG. S17: Fluctuations of gas-phase VEGs as QM/BioEFP VEGs increase. Gas-phase calculations were performed at the 6-31G(d)/LANL2DZ/ωB97X-D level of theory in Q-Chem; the charges of the FeP ring and propionic groups were constrained using constrained DFT. R^2 values are taken from linear regression analysis, shown in black dashed lines.

S8. ADDITIONAL ELECTROSTATIC INTERACTIONS

The electrostatic interactions between the quantum subsystem and the nearby charged residues in the protein were explored to better understand the source of fluctuations in VEGs. The fluctuations in electrostatic interactions between the QM region and all charged amino acids (Lys, Arg, Asp, Glu) were not found to correlate with the fluctuations in VEGs.

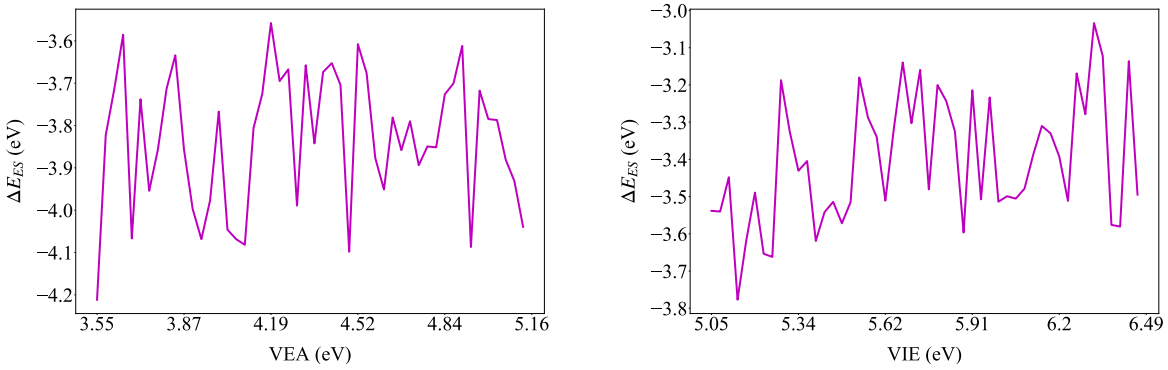

FIG. S18: Fluctuations of total electrostatic interaction energy of only charged residues in the protein (Lys, Arg, Asp, and Glu).

S9. PROTEIN RMSD

The snapshots used for calculating VEGs were chosen from last 5 ns of the 10 ns the production run MD trajectories for both states. To further explore the stability of the protein along the MD simulation, the trajectories were extended to 50 ns. The RMSD with respect to the protein backbone appears stable for the oxidized simulation; it does, however, increase around 20 ns for the simulation corresponding to the reduced HP heme. Yet, RMSD of the HP heme itself, or of the QM region with nearby residues (within 5Å and 10Å) is stable in both simulations. One can anticipate in this case that the heme and the local heme environment which can most drastically affect computed energetic parameters are not affected much by the protein dynamics even beyond the sampled region of the trajectory.

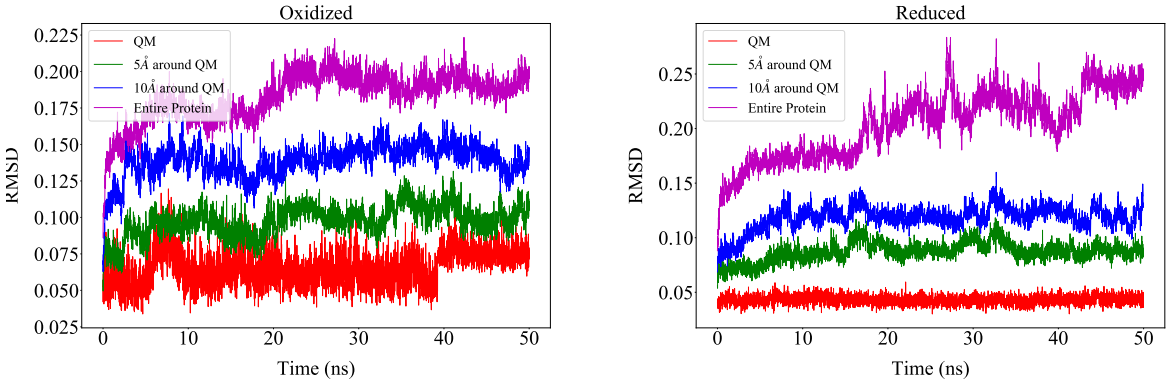

FIG. S19: Root mean squared deviations of various groups in extended oxidized and reduced trajectories, computed with GROMACS.

S10. CHOICE OF THE QM METHOD: DFT VS. SF-TDDFT

Considering multiple snapshots for which the energetic parameters have to be evaluated, using multireference methods becomes computationally prohibitive for the size of the quantum part. Therefore, less expensive alternative have been explored. The two methods considered were DFT and SF-TDDFT. As a model we considered FePMetHis system (see Fig. S9). The geometries of the neutral and the cationic states have been optimized at DFT (ωB97X/6-31G*/LANL2DZ) level. Triplet and quartet states have been chosen as a reference for the singlet and doublet states, correspondingly. Note, however, that all spin states for Fe(II) and Fe(III) can be expected to have significant multiconfigurational character. The relevant energies and $< S^2 >$ values are listed in Tables S10 and S11.

One can notice that SF-TDDFT $< S^2 >$ values for the reference and target states are close to those for the spin-pure states of the corresponding multiplicity. VIEs differ notably between DFT and SF-TDDFT results (the deviation of 0.3 eV). Yet, VEA are very close (within 0.1 eV). Linear response (LR) estimates of AIE ($0.5(VIE + VEA)$) are within $\sim$0.2 eV of each other at DFT and SF-TDDFT level. As AIE and LR AIE are the quantities that are most closely related to the Gibbs free energy of the oxidation, one can expect that the differences in computed estimates of the free energies between two methods will be within 0.1 - 0.2 eV. Considering that the SF-TDDFT is more computationally expensive and that the total energies of the singlet and doublet states are lower at DFT level, DFT was a method of choice for all QM calculations in this work.

TABLE S10: Total energies, $< S^2 >$, VIEs, VEAs, and AIEs computed with SF-TDDFT (ωB97X/6-31G*/LANL2DZ in both cases).

Geometry			
Neutral, (Fe(II))		Cation, (Fe(III))	
SF-TDDFT, ωB97X/6-31G*/LANL2DZ			
Total energy, a.u.			
Singlet	Doublet	Singlet	Doublet
-1815.727060	-1815.520964	-1815.724401	-1815.519503
Reference state $< S^2 >$			
Triplet	Quartet	Triplet	Quartet
2.02	3.88	2.02	3.89
Target state $< S^2 >$			
Singlet	Doublet	Singlet	Doublet
0.12	0.94	0.11	0.95
VIE, eV		VEA, eV	
5.61		5.58	
AIE, eV			
5.65			
LR AIE ($\frac{1}{2}(VIE + VEA)$), eV			
5.59			

TABLE S11: Total energies, $< S^2 >$, VIEs, VEAs, and AIEs computed with DFT (ωB97X/6-31G*/LANL2DZ).

Geometry			
Neutral, (Fe(II))		Cation, (Fe(III))	
DFT, ωB97X/6-31G*/LANL2DZ			
Total energy, a.u.			
Singlet	Doublet	Singlet	Doublet
-1815.765097	-1815.547400	-1815.763646	-1815.553869
$< S^2 >$			
Singlet	Doublet	Singlet	Doublet
0.00 (RDFT)	0.89	0.00 (RDFT)	0.83
VIE, eV		VEA, eV	
5.92		5.71	
AIE, eV			
5.75			
LR AIE ($\frac{1}{2}(VIE + VEA)$), eV			
5.82			

[1] N. Foloppe and A. MacKerell, *J. Comput. Chem.*, 2000, **21**, year.

[2] A. D. MacKerell, D. Bashford, M. Bellott, R. L. Dunbrack, J. D. Evanseck, M. J. Field, S. Fischer, J. Gao, H. Guo, S. Ha, D. Joseph-McCarthy, L. Kuchnir, K. Kuczera, F. T. K. Lau, C. Mattos, S. Michnick, T. Ngo, D. T. Nguyen, B. Prodhom, W. E. Reiher, B. Roux, M. Schlenkrich, J. C. Smith, R. Stote, J. Straub, M. Watanabe, J. Wiórkiewicz-Kuczera, D. Yin and M. Karplus, *J. Phys. Chem. B*, 1998, **102**, 3586–3616.

[3] F. Autenrieth, E. Tajkhorshid, J. Baudry and Z. Luthey-Schulten, *J. Comput. Chem.*, 2004, **25**, 1613–1622.

[4] H. Shimizu, D. J. Schuller, W. N. Lanzilotta, M. Sundaramoorthy, D. M. Arciero, A. B. Hooper and T. L. Poulos, *Biochemistry*, 2001, **40**, 13483–13490.

[5] S. Pronk, S. Páll, R. Schulz, P. Larsson, P. Bjelkmar, R. Apostolov, M. R. Shirts, J. C. Smith, P. M. Kasson, D. van der Spoel, B. Hess and E. Lindahl, *Bioinformatics*, 2013, **29**, 845–854.

[6] Y. Shao, Z. Gan, E. Epifanovsky and et. al., *Mol. Phys.*, 2015, **113**, 184–215.

[7] L. Li, C. Li, S. Sarkar, J. Zhang, S. Witham, Z. Zhang, L. Wang, N. Smith, M. Petukh and E. Alexov, *BMC Biophys.*, 2012, **5**, 1682–5–9.

[8] D. W. Scott, *Biometrika*, 1979, **66**, 605–610.

[9] D. W. Scott, *WIREs Comp. Stat.*, 2010, **2**, 497–502.

[10] D. W. Scott, *Sturges' and Scott's Rules*, Springer Berlin Heidelberg, Berlin, Heidelberg, 2011, pp. 1563–1566.

[11] H. A. Sturges, *Journal of the American Statistical Association*, 1926, **21**, 65–66.

[12] S. J. Sheather, *Statistical Science*, 2004, **19**, 588–597.

[13] D. W. Scott, *WIREs Computational Statistics*, 2010, **2**, 160–164.

[14] S. L. Anderson, E. J. Luber, B. C. Olsen and J. M. Buriak, *Chemistry of Materials*, 2016, **28**, 5973–5975.

[15] J. Chu, M. González-López, S. L. Cockroft, M. Amorin and M. R. Ghadiri, *Angewandte Chemie International Edition*, 2010, **49**, 10106–10109.

[16] C. Barroo, Y. De Decker, T. Visart de Bocarmé and P. Gaspard, *J. Phys. Chem. Lett.*, 2015, **6**, 2189–2193.

[17] B. Cao, X. He, C. R. Fetterly, B. C. Olsen, E. J. Luber and J. M. Buriak, *ACS Applied Materials*

& Interfaces, 2016, **8**, 18238–18248.

[18] H. Li, A. Munk, H. Sieling and G. Walther, *Biometrika*, 2020, **107**, 347–364.

[19] D. Chakraborty, K. Berland and T. Thonhauser, *Journal of Chemical Theory and Computation*, 2020, **16**, 5893–5911.

[20] C. J. Olea, J. Kuriyan and M. A. Marletta, *J. Am. Chem. Soc.*, 2010, **132**, 12794–12795.

[21] S. Neya, M. Suzuki, T. Hoshino, H. Ode, K. Imai, T. Komatsu, A. Izezaki, M. Nakamura, Y. Furutani and H. Kandori, *Biochemistry*, 2010, **49**, 5642–5650.

[22] Y. Imada, H. Nakamura and Y. Takano, *J. Comput. Chem.*, 2018, **39**, 143–150.